Directional characteristics of spatially evolving young waves under steady wind

Krishanu Kumar, Santosh Kumar Singh,* and Lev Shemer†
Tel Aviv University, School of Mechanical Engineering, Tel Aviv 6997801, Israel

(Received 28 July 2021; accepted 10 January 2022; published 24 January 2022)

Synchronous single point measurements of the instantaneous surface elevation and of two components of the surface slope in a wind-wave tank are carried out using a high-speed camera and a laser slope gauge. The applied technique allows study of joint statistics between the temporal variation of surface elevation and the slope components at a point, as well as computation of directional wave energy spectra. It is demonstrated that while significant coherence exists between surface elevation and along-wind slope component, the coherence between crosswind slope and surface elevation is almost negligible. Evolution of the directional spectra along the test section is presented for different wind velocities and compared with results obtained in other relevant field and laboratory studies.

DOI: 10.1103/PhysRevFluids.7.014801

I. INTRODUCTION

Generation of water waves by wind involves multiple physical processes characterized by a range of temporal and spatial scales. Understanding of those processes is crucial not only for fundamental scientific studies but also for engineering applications that require accumulation of large amount of reliable and accurate experimental data. Power spectra of waves in ocean and in laboratory are most commonly measured by different types of wave gauges that are insensitive to wave propagation direction. Information on wave orientation can be obtained from imaging of large sea areas, mostly by different types of radars. Versions of synthetic aperture radar (SAR) including polarimetric SAR [1], interferometric SAR [2], as well as nautical radars [3] are used for this purpose. The spatial resolution of radar images is, however, limited. Optical techniques such as stereo imaging of sea surface from sea platforms introduced by Banner *et al.* [4] and developed significantly since then [5] offer great promise as they potentially are capable of providing much better spatial and temporal resolution as compared to radar imaging. However, the area covered by video cameras is limited and thus relatively short sea waves are visualized. Reconstruction of well-resolved data from the images requires substantial computer resources, which may affect the practically available resolution in space and time [6].

Alternatively, directional information on waves can be extracted from single- and multipoint arrays of sensors (see Refs. [7,8] and references therein). The spacing between sensors in the array puts a limit on the maximum measurable wavelength. Simultaneous single point measurements of several wave parameters using wave buoy or pressure pads allow to circumvent this difficulty [9–14]. In spite of advances in application of diverse measurement techniques over the years, they all have significant limitations. Detailed field measurements of wind-waves are challenging not only because they are necessarily complicated and expensive but also due to unsteady and

*Present address: Department of Mechanical Engineering, SRM Institute of Science and Technology, Kattankulathur, Chennai 600036, India.
†shemerl@tauex.tau.ac.il

unpredictable environmental and wind forcing conditions. The considerable difficulties inherent to field experiments lead to uncertainties in application of the accumulated data as a basis for wind-wave modeling and for validation of theoretical models.

Laboratory wind-waves studies are less expensive and offer an advantage of full control of the system as compared to field studies, thus allowing us to perform accurate and well-resolved measurements. However, waves in laboratory facilities are much shorter than in the sea. Additional issues that may be important in performing laboratory studies of wind-waves as compared to those in nature are discussed in detail in Ref. [15]. Extensive measurements of spatially evolving wind-waves under steady wind forcing carried out in our moderately sized experimental facility, Refs. [16–18] documented the growth of wind-wave amplitudes and downshifting of peak frequencies along the test section for a wide range of wind velocities. It was demonstrated that the measured dependencies of both dimensionless amplitudes and dimensionless dominant frequencies on the dimensionless fetch are in good agreement with results obtained in a much larger facility and in field. These studies also showed that properly normalized wave power spectra at different fetches and wind velocities fall on a single. Joint North Sea Wave Project (JONSWAP) spectral shape [19], thus demonstrating that measurements in limited-size facilities can shed light on mechanisms governing wind-wave behavior at much larger scales.

Although waves in a laboratory tank are excited by unidirectional steady wind, they are random and short crested, so that the water surface is essentially three dimensional. To analyze their three-dimensional structure, stereo video imaging was applied [20]. Comparison of the data extracted from the three-dimensional (3D) reconstruction of the wave field with reliable single point measurements by a wave gauge showed that stereo video imaging is capable of presenting the global features of the wave field with reasonable accuracy. However, the procedure fails in detection of more subtle features, partially due to space limitations but mainly since the computer power requirements could not be met adequately. A different approach based on a laser slope gauge (LSG) allows measurements of temporal variation of two components of the instantaneous surface slope, $\partial\eta/\partial x(t)$ and $\partial\eta/\partial y(t)$ [21]. The surface elevation $\eta(t)$ was measured by a capacitance-type wave gauge at a nearby location. Those measurements provide significant statistical information on three-dimensional structure of wind-waves; however, coherence between surface elevation and its orthogonal slope components could not be established.

In the present study, a nonintrusive optical instrument is used to investigate directional properties of young wind waves in a laboratory tank. Synchronous single-point measurements of the surface elevation $\eta(t)$ by a high-speed camera and of the along-wind, $\partial\eta/\partial x(t)$, and cross-wind, $\partial\eta/\partial y(t)$, slope components by LSG are performed under various wind forcing conditions. Those measurements allow gaining information on the coherence and on the phase relations between the measured parameters. Moreover, simultaneous measurements of η and of $\partial\eta/\partial x$ and $\partial\eta/\partial y$ allow determination of two-dimensional directional spectra in a laboratory facility. Measurements are performed for different fetches and wind velocities. The capabilities of the measuring technique employed in the present experiments are compatible with buoy so that the mathematical procedure proposed for buoy measurements by Longuet-Higgins *et al.* [9] can be applied. The technique is applicable in laboratory environment and has the advantage of direct surface elevation determination by the camera rather than by integration of the accelerometer data in the buoy measurements.

II. EXPERIMENTAL SETUP AND PROCEDURE

The experiments were performed in a wind-wave flume that consists of a closed-loop wind tunnel atop a 5 m long, 0.4 m wide, and 0.5 m high test section made of glass and filled with distilled water; the water depth of 0.20 m satisfies deep-water conditions for wavelengths in the experiments. A sloping beach is installed to reduce wave reflection. The test section is covered by transparent removable Perspex plates. The wind is generated by a computer controlled blower. The LSG is installed on a separate movable frame, so that the instantaneous surface slope components can be measured at any location along the channel. The LSG setup consists of a position sensor detector

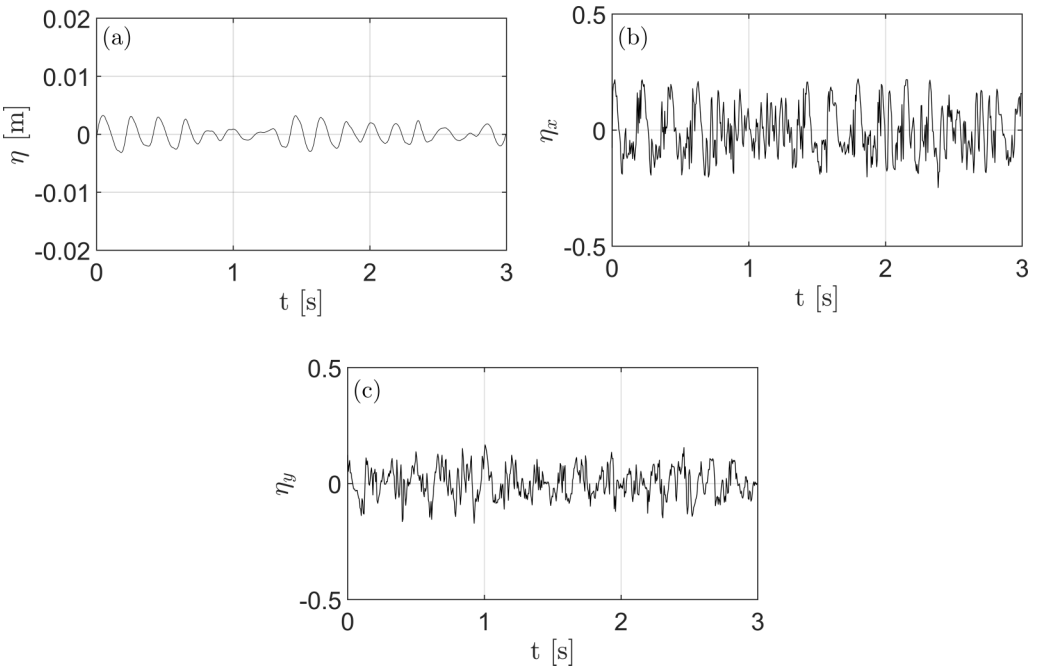

FIG. 1. Time series of (a) instantaneous surface elevation η, (b) along-wind slope η_x, and (c) crosswind slope η_y; $U = 6.3$ m/s, $x = 310$ cm.

(PSD), Fresnel lens with a 9″ focal length, diffusive screen, and a 650-nm, 200-mW laser diode. The laser is positioned under the test section and is directed vertically; the focused beam has a diameter of about 0.5 mm. The PSD records the beam location on the screen, the coordinates of this spot that are translated into the values of the instantaneous surface slope components, $\partial\eta/\partial x$ and $\partial\eta/\partial y$. For more details on the experimental facility, LSG, and its calibration see Refs. [16,17,20–22].

The laser beam that is visible in water but not in air is recorded by the high-speed complementary metal-oxide-semiconductor (CMOS) 2048 × 2048 pixel camera through the side window of the test section. The camera is synchronized with the LSG by LabView software. The vertical field of view of about 8-cm results in spatial resolution of 40 μm/pixel. The impact of ambient light is largely eliminated by imaging a narrow strip along the laser beam only. The tip of the laser beam defines the interface location, and thus the camera acts as an effective optical wave gauge that does not introduce any disturbance to the flow. The camera was viewing the beam through the side window of the test section and tilted at 30° from the horizontal plane. Synchronized records of the instantaneous surface elevation by the camera and of the two slope components by the LSG were acquired at the rate of 200 Hz for 600 s. The measurements were carried out at distances of 130, 190, 230, 270, and 310 cm from the inlet to the test section along the center line of the tank at wind velocities ranging from 4.1 to 8.5 m/s.

III. RESULTS

A. Coherence between surface elevation and slope components

An example of simultaneously recorded at a single point surface elevation $\eta(t)$ and its slope components $\eta_x(t)$ and $\eta_y(t)$, presented in Fig. 1 demonstrates that these three records apparently have a similar dominant frequency of about 5 Hz. The amplitude of fluctuations of $\eta_y(t)$ is smaller but comparable to that of $\eta_x(t)$, indicating that wind waves are three dimensional. High-frequency

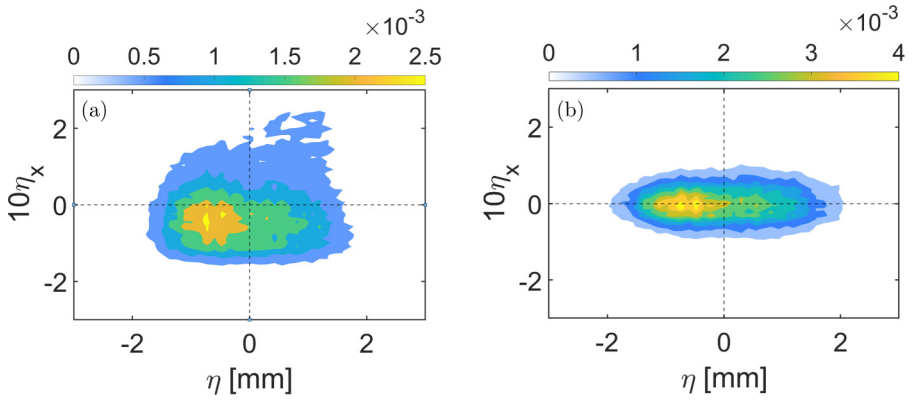

FIG. 2. Joint probability density function between η and (a) η_x and (b) η_y; $U = 6.3$ m/s and $x = 310$ cm.

capillary waves riding on front face of large-amplitude gravity waves are clearly visible in records of η_x and η_y, Figs. 1(b) and 1(c). These steep small-amplitude waves cannot be identified in the surface elevation record due to the finite camera resolution; thus the temporal variation of η in Fig. 1(a) is much smoother than the LSG-derived records of slope components. The frequency spectra of $\eta(t)$, measured by a capacitance gauge, as well as of $\eta_x(t)$ and $\eta_y(t)$ were plotted and discussed in detail in Ref. [21] and therefore are not presented here.

Single-point measurements allow to calculate joint probability density functions (*jpdf*) for the pairs η-η_x and η-η_y; typical examples of those *jpdf*'s that represent 120,000 instantaneous values of both parameters in each pair are presented in Fig. 2. The shapes of *jpdf*'s of η-η_x and η-η_y are quite different. The most probable surface elevation in Fig. 2, $\eta_{\rm mp} = -0.66$ mm is slightly negative. This is attributed to nonlinearity of wind-waves that leads to sharper (and shorter) crests and longer (and flatter) troughs. The most probable value of η_x that is also negative, Fig. 2(a), is associated with the vertical asymmetry of wind waves with shorter leeward and longer windward face. The skewness coefficient of the instantaneous surface elevation is positive, in agreement with Zavadsky and Shemer [21]. The *jpdf* of η-η_y in Fig. 2(b) is thinner than that in Fig. 2(a) due to a smaller range of variation of the cross-wind slope η_y; it is symmetric with respect to the horizontal axis. This indicates that the surface elevation slope in the cross-wind direction is only weakly correlated with η.

The accumulated data enable studying the correlation between the possible pairs of the measured parameters. The cross-correlation coefficient $R_{fg}(\tau)$ between two functions with zero mean, $f(t)$ and $g(t)$, is defined for time shift τ as [23]:

$$R_{fg}(\tau) = \frac{\overline{f(t)g(t+\tau)}}{\overline{f^2}^{1/2}\overline{g^2}^{1/2}}. \tag{1}$$

To obtain statistically reliable estimates of R, the records of η, η_x, and η_y are divided into synchronous parts with duration of 10 local characteristic wave periods $T_p = 1/f_p$ long, resulting in few hundred independent segments. The peak frequency f_p is estimated from the power spectra of the surface elevation $\hat{\eta}(f)$ by fitting a parabola in the ± 1 Hz vicinity of the spectral peak of $\hat{\eta}$. The peak frequency of the surface elevation is always somewhat lower than that of the along-wind slope component η_x [21]. Due to fast decay of the cross-correlation coefficients $R(\tau)$, it was sufficient to calculate them for $0 \leqslant \tau \leqslant 1\,s$; the results for each operational condition were then averaged over all segments. The averaged curves of $R(\tau)$ are plotted in Fig. 3 for $U = 6.3$ m/s and three fetches for η-η_x and η-η_y; in each plot the time delay τ is normalized by T_p. The coherence coefficients decay fast within few dominant wave periods; that is consistent with the limited temporal coherence of wind waves [24]. The maximum values of $R_{\eta\eta_y}$ are significantly smaller than those of $R_{\eta\eta_x}$; this

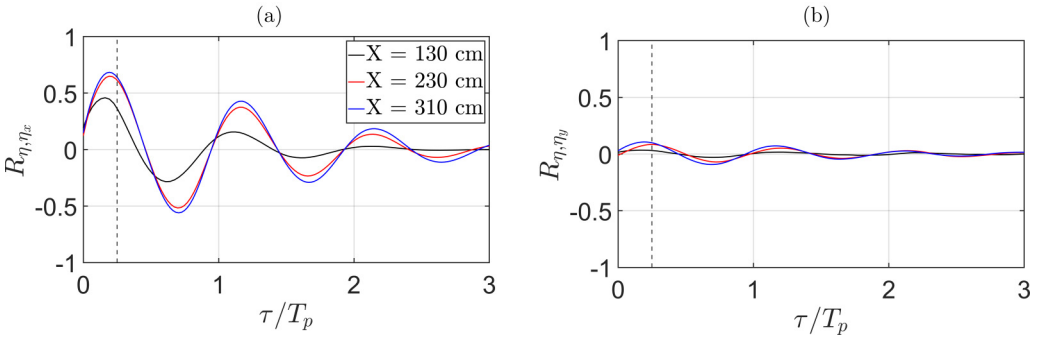

FIG. 3. Cross-correlation function between η and (a) η_x and (b) η_y; $U = 6.3$ m/s; dashed line: $\tau/T_p = 0.25$.

supports the conjecture that the cross-wind slope component η_y is effectively uncorrelated with the surface elevation η. The normalized time lag corresponding to the peak correlation value τ_p/T_p in Fig. 3(a) is less than 0.25; normalization of τ by the slightly shorter characteristic period of η_x rather than that of η does not change the pattern notably.

Visual inspection of synchronous records of $\eta(t)$, $\eta_x(t)$, and $\eta_y(t)$ suggests a possibility of temporal variability in coherence between those records. For example, while Fig. 3(b) shows that $\eta(t)$ and the crosswind slope $\eta_y(t)$ are almost uncorrelated, short apparently coherent stretches were observed in the records presented in Figs. 1(a) and 1(c). To examine this possible intermittency, the statistics of the peak values of $R_{\eta\eta_x}$ and of $R_{\eta\eta_y}$, as well as of the corresponding normalized time-lags τ_p/T_p obtained for each pair of multiple short segments, are further analyzed. Examples of *pdf* of peak values of the cross correlation coefficients and of the corresponding values of τ_p/T_p calculated for ensembles of short segments as in Fig. 3 are presented in Figs. 4(a) and 4(c) and Figs. 4(b) and 4(d). The most probable values of $R_{\eta\eta_x}$ exceed significantly those of $R_{\eta\eta_y}$; both increase with fetch. The width of the distribution of the peak values of $R_{\eta\eta_x}$ apparently does not depend on fetch x, while the corresponding distribution width for $R_{\eta-\eta_y}$ widens significantly. Hence, for short stretches of time, the correlation between η-η_y can be nearly as high as for η-η_x. The most probable dimensionless time-lag for η-η_x is quite close to its peak value, see Fig. 3(a); however, the corresponding *pdf* for η-η_y is wide with no pronounced maximum, as expected for the lack of significant coherence between η and η_y.

The coherence between two signals in the frequency domain is assessed using the magnitude-square coherence, MSC(f):

$$\mathrm{MSC}(f) = \frac{|S_{\eta,\eta_x}(f)|^2}{S_{\eta\eta}(f)S_{\eta_x\eta_x}(f)}, \tag{2}$$

where $S_{\eta\eta}$ and $S_{\eta_x\eta_x}$ are the autospectral densities of the surface elevation $\eta(t)$ and of along-wind slope $\eta_x(t)$; $|S_{\eta\eta_x}|$ is the absolute value of their cross-spectral density [23]. The distributions of MSC(f) for three fetches x and two wind velocities U are plotted in Figs. 5(a)–5(c). The peak frequencies f_p of the spectra of the surface elevation $\eta(t)$ and of the slope component $\eta_x(t)$ are also presented in those panels by vertical lines. Figure 5 shows that, for each experimental condition, η and η_x are best correlated in the vicinity of the peak frequencies f_p of $\eta(t)$ and of $\eta_x(t)$ where the values of MSC exceed 0.9.

The phase shift between η and η_x is determined from the complex cross-spectrum as:

$$\Delta\phi(f) = \tan^{-1}\left\{\frac{\mathrm{Im}[S_{\eta\eta_x}(f)]}{\mathrm{Re}[S_{\eta\eta_x}(f)]}\right\} \tag{3}$$

and presented in Fig. 6 for frequencies at which η and η_x are correlated reasonable well, so that MSC > 0.5.

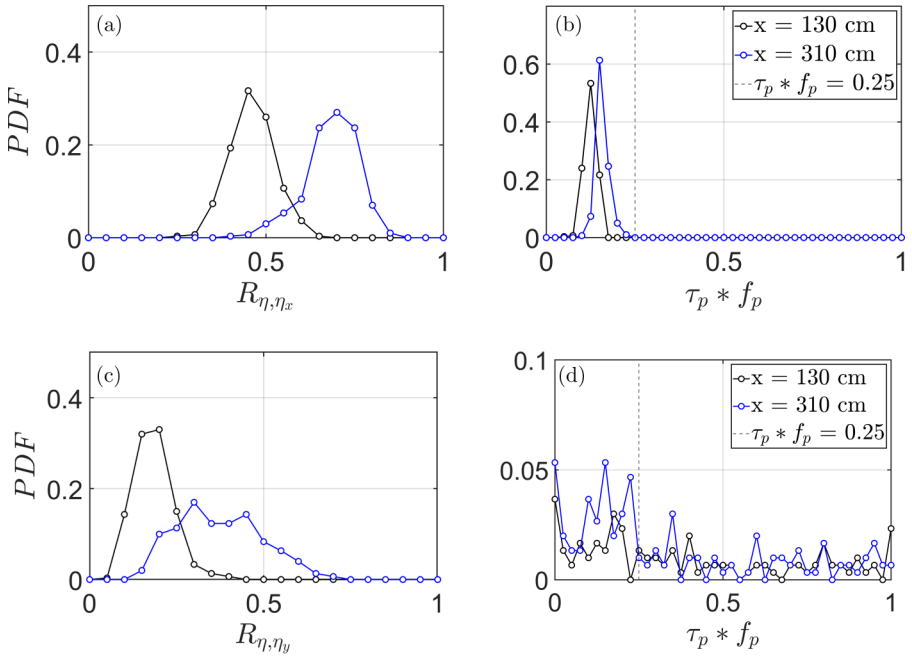

FIG. 4. Probability distribution function (*pdf*) of [(a) and (c)] peak correlation value and [(b) and (d)] nondimensional lag (τ_p/T_p); between η and η_x (upper row); between η and η_y (lower row); for $U = 6.3$ m/s.

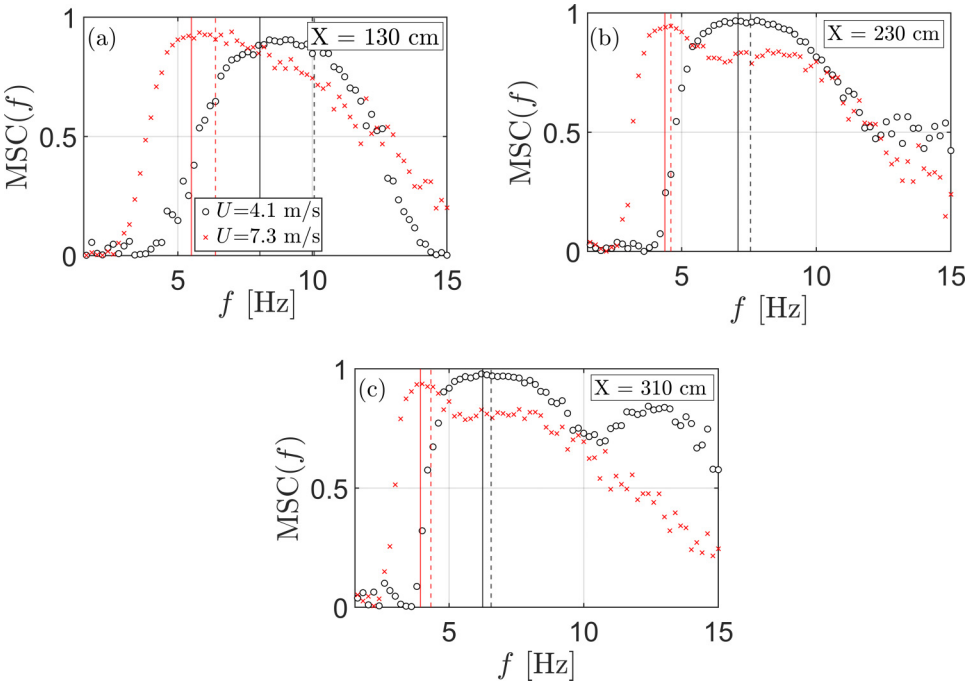

FIG. 5. Magnitude squared coherency, MSC(f), of η and η_x at (a) $x = 130$ cm, (b) $x = 230$ cm, and (c) $x = 310$ cm. Vertical lines: solid f_p of η; dashed f_p of η_x.

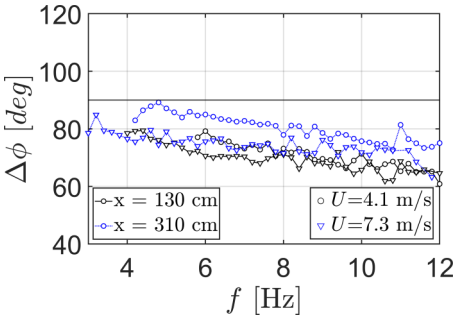

FIG. 6. Phase difference between η and η_x, $\Delta\phi(f)$; (black) $x = 130$ cm and (blue) $x = 310$ cm.

At all frequencies in Fig. 6, the phase shifts between the corresponding frequency harmonics of η and η_x are below $\Delta\phi = 90^\circ$ expected for coherent linear waves and are only weakly dependent on x and U, although downward trend with f and with wind velocity may be noticed. The deviation from the linear value may be attributed to somewhat different peak frequencies of η and η_x and to the fast loss of coherence of those random signals, as demonstrated in Figs. 3 and 4. It is consistent with the normalized by the wave period time lag that is consistently below 0.25 associated with $\Delta\phi = 90^\circ$, see Fig. 4(b).

B. Directional spreading

Single point measurement of surface elevation $\eta(t)$, upwind-downwind slope $\eta_x(t)$, and cross-wind slope $\eta_y(t)$ enable estimation of the directional spectra of wind-waves in the facility. The two-dimensional energy spectrum $\hat{S}(f,\theta)$ where θ is the propagation angle, is customarily presented as a product of the omnidirectional power spectrum of $\eta(t)$ and the directional spreading function $D(f,\theta)$. Following Longuet-Higgins *et al.* [9], the spreading function is estimated as

$$D(f,\theta) = 2^{2s(f)-1}\frac{\Gamma^2[s(f)+1]}{\pi\Gamma[2s(f)+1]}\cos^{2s(f)}\frac{\theta-\theta_0}{2}, \tag{4}$$

where Γ is the gamma function, θ_0 is the mean propagation direction taken as $\theta_0 = 0^\circ$ along the test section in the wind direction, and $s(f)$ is total spreading parameter calculated as the average of first-order, $s_1(f)$, and second-order, $s_2(f)$, spread parameters:

$$s_1(f) = \frac{r_1(f)}{1-r_1(f)}; \quad s_2 = \frac{1+3r_2(f)+[1+14r_2(f)+r_2(f)^2]^{1/2}}{2[1-r_2(f)]}. \tag{5}$$

The functions $r_1(f)$ and $r_2(f)$ are computed using the following equations:

$$r_1(f) = \frac{\left[a_1^2(f)+b_1^2(f)\right]^{1/2}}{a_0(f)}; \quad r_2(f) = \frac{\left[a_2^2(f)+b_2^2(f)\right]^{1/2}}{a_0(f)}, \tag{6}$$

where the coefficients $a_0(f)$, $a_1(f)$, $b_1(f)$, $a_2(f)$, and $b_2(f)$ are based on the co- and quadrature spectra of $\eta(t)$, $\eta_x(t)$, and $\eta_y(t)$; the corresponding lengthy expressions are presented in [25]. The spreading parameter s controls the angular distribution of $\hat{S}(f,\theta)$. The first-order parameter s_1 contains contributions of the spectra of η and of the cross-spectra between η and the two slope components, while the second-order parameter s_2 contains only spectra and cross-spectra of η_x and η_y. The parameters s_1 and s_2 are equal at all frequencies when the relation between the functions r_1 and r_2 follows the dashed line plotted in Fig. 7(a). The measured values of r_1 and r_2 at all harmonics are presented in this figure for different wind velocities and for various fetches; in each record computations of the co- and cross-spectra are carried out separately for multiple 10-s-long synchronous records of the measured parameters. The data points are consistently above the dashed

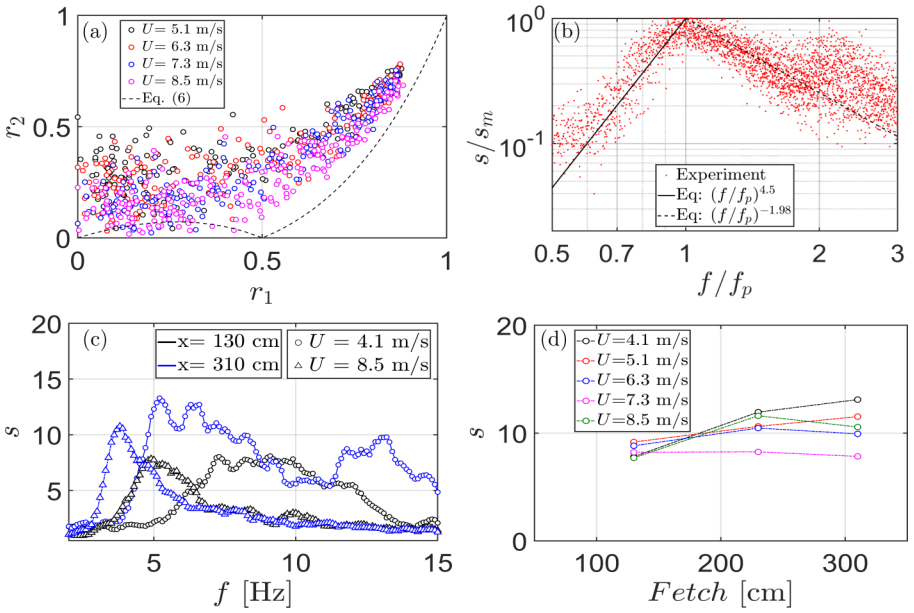

FIG. 7. (a) Comparison between measured values of r_1 and r_2, (b) The normalized spreading parameter s/s_m as a function of the dimensionless frequency f/f_p, (c) spreading parameter $s(f)$, and (d) variation of peak spreading parameter s_m along the channel.

line, resulting in $s_2 > s_1$, in agreement with Refs. [11,26–28]. The spreading parameter normalized by its maximum value, s/s_m, is presented in Fig. 7(b) for all values of wind velocities and fetches as a function of dimensionless frequency f/f_p, f_p being the spectral peak frequency of η. The frequency dependence of s/s_m is usually approximated as $s/s_m = (f/f_p)^n$, where n is a dimensionless constant. For frequency range $f/f_p < 1$, the exponent n in Fig. 7(b) is approximately 4.5, while for $f/f_p > 1$, $n \approx -1.98$. Those values are comparable with the results of field measurements [10] who obtained $n = 5$ for $f/f_p < 1$ and $n = -2.5$ for $f/f_p > 1$.

Higher values of the spreading parameter s correspond to narrower angular distribution, see Eq. (4). The spreading parameter $s(f)$ is presented in Fig. 7(c) at two extreme location for $U = 4.1$ m/s and 8.5 m/s. The experimentally determined function $s(f)$ has considerable scatter; hence, Savitzky-Golay filter is applied. Note the shape of $s(f)$ resembles that of the MSC(f), Figs. 5(a) and 5(c); both attain maximum in the vicinity of the spectral peak frequency f_p of η. The wide distribution of $s(f)$ at a shorter fetch becomes more concentrated at longer fetches. At low wind velocities and larger fetches, the spreading function exhibits notable peak at the second harmonic $2f_p$ that is apparently associated with the second-order bound waves. The maximum values of s_m obtained by fitting a parabola in the vicinity (± 0.5 Hz) at f_p are presented as a function of fetch for different wind velocities in Fig. 7(d). At the low wind velocity of $U = 4.1$ m/s, the maximum spreading parameter s_m increases with fetch, while for stronger winds, no clear trend in dependence of s_m on fetch or wind velocity can be identified.

The two-dimensional energy spectra $\hat{S}(f, \theta)$ at different fetches and wind velocities are presented in Fig. 8. The spectra are calculated with resolution of 0.1 Hz in frequency and of 1° in the propagation direction. As expected, all spectra are symmetric, with the spectral peak corresponding to the wind direction $\theta = 0°$. The power at the peak increases with fetch (for constant U), and with the wind velocity (for constant fetch). Similarly, the peak frequency decreases with x and with U. Measurements of temporal evolution of wind-wave directional spectra in an annular wave flume [29] demonstrated similar wave energy growth, frequency downshifting and decrease in directional spreading with time. These results are also consistent with behavior of the spreading coefficient

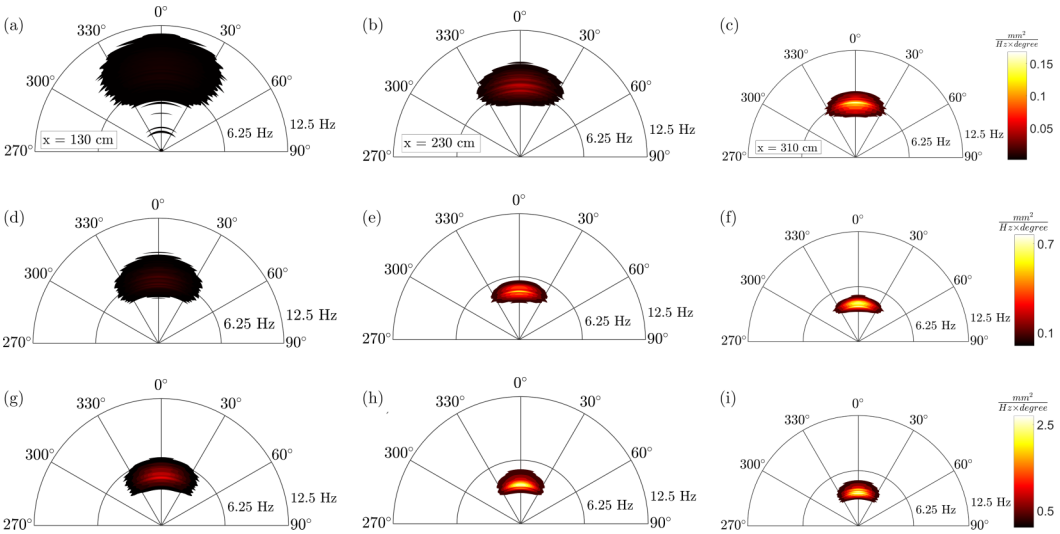

FIG. 8. Two-dimensional energy spectrum $\hat{S}(f,\theta)$ at $x = 130$, 230, and 310 cm and $U = 4.1$ m/s (first row); $U = 6.3$ m/s (second row), and $U = 8.5$ m/s (third row).

s in Fig. 7(c), at each wind velocity U, the angular spreading decreases with fetch (the rows of Fig. 8), while for a constant fetch x the spreading decreases with U (the columns of Fig. 8). Note that contrary to field measurements where the wind-wave angular spreading may be affected by the directional spreading of the forcing wind, the wind in laboratory experiments is unidirectional. The observed spreading thus characterizes the intrinsic feature of wind-waves.

IV. DISCUSSION AND CONCLUSION

Wind-waves are commonly studied by measuring surface elevation at fixed points in space. Such measurements enable computation of omnidirectional power spectra that reveal the wave energy distribution among the spectral frequencies. However, single point measurements provide only limited information on wind-induced surface waves that always exhibit directional spreading. A nonintrusive optical method developed here allows filling of this gap, in particular in laboratory investigations of young wind-waves. The experimental approach is based on synchronous measurements of instantaneous surface elevation $\eta(t)$ and its orthogonal slope components, $\eta_x(t)$ and $\eta_y(t)$, at a single point using a vertical laser beam and synchronized high-speed camera and 2D LSG. The vertical laser beam used in the LSG is visible only in water [30], thus the instantaneous location of the upper tip of the beam recorded by the camera corresponds to the air-water interface $\eta(t)$. Note that measurements based on conventional wave-gauges that interfere with the laser beam are incapable of providing information on coherence and phase-relation between the surface elevation η and its slope components η_x and η_y. To eliminate occasional instantaneous strong surface curvature at strong winds that may result in direct hit of the camera lens by the deflected beam, the maximum wind velocity in the present study did not exceed 8.5 m/s.

The maximum values of the cross correlation coefficients between η and η_x exceed 0.5 and are notably higher than those between η and η_y; yet they remain significantly smaller than unity. The values of the magnitude squared coherence presented in Fig. 5 nevertheless demonstrate that these cross-coherence coefficients exceed 0.9 around the peak frequencies of $\hat{\eta}$ and $\hat{\eta}_x$. The relatively high coherence between η and η_x decays quite fast in time, within a few dominant wave periods, in agreement with the temporal behavior of the corresponding autocorrelation coefficients [24]. The phase difference between η and η_x that lose coherence fast remains below 90° at all frequencies.

The values of $R_{\eta\eta_y}$ obtained by averaging over the whole recording duration show lack of coherence between those signals even at short time delays τ. However, significant maximum values of $R_{\eta\eta_y}$ that may be obtained for relatively short segments of the full records, see Fig. 4(c), suggest that while η and η_y may be intermittently partially correlated, their phase relations in different short segments in the ensemble vary randomly, resulting in the symmetric shape of the joint probability density function $jpdf$ between η-η_y.

Additional important benefit from single point synchronous measurements of the temporal variation of $\eta(t)$ and of the two surface slope components is the possibility to compute the directional wave energy spectra. To the best of our knowledge, spatial evolution of those spectra have not been measured in laboratory facilities so far. Unlike in field experiments, the mean wind velocity in the test section of a wind-wave tank retains its direction, thus allowing characterization of the directional spreading as the intrinsic property of wind waves and decoupling it from the variability of the wind direction inevitable in large scale measurements. The parameters measured directly in the present experiments are identical to those provided by a buoy, but have a better spatial and temporal resolution; since the method is optical, they are not affected by inertia. The analogy with buoy measurements allowed to compute directional spectra using mathematical procedure initially proposed by Longuet-Higgins *et al.* [9] and then further developed in subsequent buoy studies [10,12,13]. In addition to the directional spectra for different fetches and wind velocities presented in Fig. 8, the spreading parameter which controls the angular energy distribution for different wind forcing conditions was also computed, see Fig. 7(b). In spite of significant differences in the experimental conditions, the obtained results are in a reasonable agreement with field measurements of Mitsuyasu *et al.* [10]. This confirms the accuracy of the method and provides further evidence that meaningful results on wind-waves evolution can be obtained in a modestly sized facility.

ACKNOWLEDGMENT

This work was supported by the Israel Science Foundation (Grant No. 508/19).

[1] D. Schuler, J. Lee, D. Kasilingam, and E. Pottier, Measurement of ocean surface slopes and wave spectra using polarimetric sar image data, Remote Sens. Environ. **91**, 198 (2004).

[2] M. Marom, E. Thornton, R. Goldstein, and L. Shemer, Remote sensing of ocean wave spectra by interferometric synthetic aperture radar, Nature (Lond.) **345**, 793 (1990).

[3] H. Dankert, J. Horstmann, W. Koch, and W. Rosenthal, Ocean wind fields retrieved from radar-image sequences, J. Geophys. Res. **108**, 2150 (2002).

[4] M. Banner, I. Jones, and J. Trinder, Wavenumber spectra of short gravity waves, J. Fluid Mech. **198**, 321 (1989).

[5] A. Benetazzo, F. Fedele, G. Gallego, P. C. Shih, and A. Yezzi, Offshore stereo measurements of gravity waves, Coast. Eng. **64**, 127 (2012).

[6] F. Bergamasco, A. Benetazzo, J. Yoo, A. Torsello, F. Barbariol, J. Y. Jeong, J. S. Shim, and L. Cavaleri, Toward real-time optical estimation of ocean waves' space-time fields, Comput. Geosci. **147**, 104666 (2021).

[7] I. R. Young, On measurement of directional wave spectra, Ocean Res. **16**, 283 (1994).

[8] I. R. Young, L. A. Verhagen, and M. L. Banner, A note on the bimodal directional spreading of fetch limited wind waves, J. Geophys. Res. **100**, 773 (1995).

[9] M. Longuet-Higgins, D. Cartwright, and N. Smith, Observations of the directional spectrum of sea waves using motions of a floating buoy, in *Ocean Wave Spectrum* (Prentice-Hall, Hoboken, NJ, 1961), 111.

[10] H. Mitsuyasu, F. Tasai, T. Suhara, S. Mizuno, M. Ohkusu, T. Honda, and K. Rikhshi, Observations of the directional spectrum of ocean waves using a cloverleaf buoy, J. Phys. Oceanogr. **5**, 750 (1975).

[11] D. Hasselmann, M. Dunckel, and J. Ewing, Directional wave spectra observed during jonswap 1973, J. Phys. Oceanogr. **10**, 1264 (1980).

[12] H. Rapizo, A. Babin, E. Schulz, M. Hemer, and T. Durrant, Observation of wind-waves from a moored buoy in the southern ocean, Ocean Dynam. **65**, 1275 (2015).
[13] T. H. C. Herbers, P. F. Jessen, T. T. Janssen, D. B. Colbert, and J. H. MacMahan, Observing ocean surface waves with gps-tracked buoys, J. Atmos. Ocean. Technol. **29**, 944 (2012).
[14] M. Latheef and D. Kim, Directional spreading resolution from point measurements for mixed seas and sea states with frequency dependent spreading, Ocean Eng. **229**, 108933 (2021).
[15] L. Shemer, On evolution of young wind-waves in time and space, MDPI Atmos. **10**, 562 (2019).
[16] D. Liberzon and L. Shemer, Experimental study of the initial stages of wind waves' spatial evolution, J. Fluid Mech. **681**, 462 (2011).
[17] A. Zavadsky, D. Liberzon, and L. Shemer, Statistical analysis of the spatial evolution of the stationary wind wave field, J. Phys. Oceanogr. **681**, 65 (2013).
[18] L. Shemer, S. Singh, and A. Chernyshova, Spatial evolution of young wind waves: Numerical modelling verified by experiments, J. Fluid Mech. **901** (2020).
[19] K. Hasselmann, T. Barnett, E. Bouws, H. Carlson, D. Cartwright, K. Enke, J. Ewing, H. Gienapp, D. Hasselmann, P. Kruseman, A. Meerburg, P. Muller, D. Olbers, K. Richter, W. Sell, and H. Walden, Measurements of wind-wave growth and swell decay during the joint north sea wave project (JONSWAP), Deut. Hydrogr. Z. **8**, 1 (1973).
[20] A. Zavadsky, A. Benetazzo, and L. Shemer, Study of spatial variability of short gravity waves in a wind wave tank by optical methods, Phys. Fluids **29**, 016601 (2017).
[21] A. Zavadsky and L. Shemer, Investigation of statistical parameters of the evolving wind wave field using a laser slope gauge, Phys. Fluids **29**, 056602 (2017).
[22] A. Zavadsky and L. Shemer, Measurements of waves in a wind-wave tank under steady and time-varying wind forcing, J. Vis. Exp. **132**, e56480 (2018).
[23] J. S. Bendat and A. G. Piersol, *Random Data: Analysis and Measurement Procedure* (John Wiley & Sons Inc., New York, 1971).
[24] L. Shemer and S. K. Singh, Spatially evolving regular water wave under the action of steady wind forcing, Phys. Rev. Fluids **6**, 034802 (2021).
[25] M. C. Huang and J. Y. Chen, Wave direction analysis from data buoys, Ocean Engng. **25**, 621 (1998).
[26] D. E. Cartwright, The use of directional spectra in studying the output of a wave recorder on a moving ship, conference on Ocean Wave Spectra, Washington, 1961, http://resolver.tudelft.nl/uuid:b6c19f1e-cb31-4733-a4fb-0f685706269b.
[27] J. A. Ewing and A. K. Laing, Directional spectra of seas near full development, J. Phys. Oceanogr. **17**, 1696 (1987).
[28] V. S. Kumar, M. C. Deo, N. M. Anand, and P. Chandramohan, Estimation of wave directional spreading in shallow water, Ocean Eng. **26**, 83 (1999).
[29] A. Toffoli, D. Proment, H. Salman, J. Monbaliu, F. Frascoli, M. Dafilis, E. Stramignoni, R. Forza, M. Manfrin, and M. Onorato, Wind Generated Rogue Waves in an Annular Wave Flume, Phys. Rev. Lett. **118**, 144503 (2017).
[30] M. A. Donelan and W. J. Plant, A threshold for wind-wave growth, J. Geophys. Res. Oceans **114**, C7 (2009).